Hybrid Incremental Nonlinear Dynamic Inversion Control with Flight Envelope Protection for Flying Wing Aircraft

Traas, T.J.J.; Atmaca, D.; van Kampen, E.

DOI
10.2514/6.2026-0549

Publication date
2026

Document Version
Final published version

Published in
Proceedings of the AIAA SCITECH 2026 Forum

AIAA SciTech Forum
12-16 January 2026, Orlando, FL
AIAA SCITECH 2026 Forum

10.2514/6.2026-0549

Hybrid Incremental Nonlinear Dynamic Inversion Control with Flight Envelope Protection for Flying Wing Aircraft

T.J.J. Traas * D. Atmaca † E. van Kampen‡
Delft University of Technology, Kluyverweg 1, 2629 HS, Delft, The Netherlands

The Flying V aircraft could revolutionize commercial aviation, boasting a potential 25% increase in aerodynamic efficiency. Due to inherent design limitations regarding static stability, a proper Flight Control System (FCS) is essential for the development of the aircraft. The concept of Hybrid Incremental Nonlinear Dynamic Inversion (INDI) was introduced to mitigate the insufficient stability margin encountered in existing sensor-based INDI systems due to sensor time delays to achieve Level 1 Handling Qualities (HQ). Furthermore, the research introduces an exponential potential function-based command limiting Flight Envelope Protection (FEP) to enhance safety compared to the currently implemented linear-based FEP. The study compares and evaluates the effectiveness of the updated system under various flight conditions and parametric uncertainties. Results show improved stability margins and a safer FEP. However, additional research is required into actuator saturation and control allocation issues during the approach condition and to enhance robustness.

I. Introduction

Despite the aviation industry's accomplishment in connecting the world, the increasing demand for air travel has its downsides, increasing awareness of environmental impacts, noise pollution, and resource depletion. The range of conventional commercial aircraft has increased by 100% in the last 50 years, but one aspect has remained the same: the aircraft layout [1]. Conventional Tube-and-Wing (CTW), as this layout is called, has the drawback that its major component, the fuselage, contributes minimally to the lift generated and significantly adds to the drag, reducing the efficiency. One promising innovation is the flying wing aircraft concept, which merges all components of a CTW into a single design. While this concept, exemplified by the B-2 Spirit, has been primarily used for military applications, its potential for commercial aviation was first proposed by Liebeck with the Blended Wing Body (BWB), promising significant reductions in take-off weight and fuel consumption [2].

Delft University of Technology has further advanced this concept with the FLYING V™§¶. This V-shaped aircraft offers flexible scalability and is comparable to an Airbus A350-900 in range and passenger capacity [3], with an expected efficiency increase of 25%, compared to an Airbus A350-900 [4]. As this type of layout has not been used previously within commercial aviation, there are still deficiencies before the Flying V can replace its predecessor CTW aircraft.

From a flight control standpoint, the objective of the Flying V project is to achieve Level 1 Handling Qualities (HQ), with the incorporation of a Flight Control System (FCS) based on MIL-STD-1797A [5], a conventional aircraft design standard. From the most recent aerodynamic analyses of the bare airframe, it was concluded that the aircraft experiences pitch break-up above Angle of Attack (AoA) of 30° [6], the Dutch Roll eigenmode is unstable [7] and there is low lateral control authority [7]. Van Overeem et al. [8] implemented an Incremental Nonlinear Dynamic Inversion (INDI), after which Stougie et al. [6] matured the FCS by looking at time delay, implementing a Flight Envelope Protection (FEP) and evaluating HQ for cruise and approach. Stougie et al. concluded that the sensor-based INDI control system did not meet the level 1 HQ requirement as time delay affected the stability margins [6]. The incorporated FEP has been tested in a piloted flight simulation and showed an overshoot for AoA and bank angle, suggesting the FEP structure should be improved [9]. Since the Flying V flight control is an active research project, there are many recent developments focusing on fault-tolerant control [10–12], new model development [13, 14], and piloted flight simulations [9, 15].

The contributions of this paper are to improve the performance of the current FCS, mature the simulation model, and increase safety by enhancing the FEP of the FCS for the Flying V aircraft. This will involve implementing a Hybrid

*MSc Student, Control and Simulation, Faculty of Aerospace Engineering
†PhD Candidate, Control and Simulation, Faculty of Aerospace Engineering; d.atmaca@tudelft.nl
‡Associate Professor, Control and Simulation, Faculty of Aerospace Engineering; e.vankampen@tudelft.nl
§Flying V is a trademark of Fortescue
¶The Flying V design is owned by Fortescue, UK & NL patents pending

INDI control law with an exponential potential function Command Limiting FEP structure and comparing it to the existing control system, which is based on a sensor-based INDI controller with a linear-based FEP [6]. Hybrid INDI is widely recognized for its capacity to address the time delay drawback associated with sensor-based INDI FCS [16, 17], improving the stability margins. Furthermore, an exponential potential function Command Limiting FEP structure is a versatile method of applying state protection [15, 18].

The structure of this paper is as follows: Section II explains the Flying V characteristics and define model properties used throughout this research. Section III defines the original control structure implemented by Stougie et al. [6] and the revised control system, highlighting the implementation of Hybrid INDI and all subsystems in the simulation model, including the updated FEP. Section IV highlights the requirements for which the control system will be tested and how these requirements are used to tune the controller. Furthermore, Section V shows and elaborates on the results of this research, highlighting the robustness of the updated Hybrid INDI control system and comparing to the linear FEP from Stougie et al. [6], with the updated FEP. Lastly, Section VI summarizes the findings of this research and advises the direction of further research regarding the challenges FCS of the Flying V, aiming to achieve the goal of level 1 HQ.

II. Flying-V Aircraft Characteristics

This section describes the characteristics of the Flying V aircraft, which are fundamental for the controller structure implementation of this research. Firstly, the dimensions and control surface layout are defined. Next, the aerodynamic model is determined, and the flight conditions and their respective trim conditions are given. Subsequently, conclusions about handling the bare airframe are described as limiting for the FCS design. Lastly, the characteristics of sensors and actuators used in this research are accompanied by the discretization method used to acquire linear models.

A. Dimensions & Control Surface Layout

The Flying V 1000, researched by Cappuyns [7], is used as a base model for this research. The dimensions of this model, with its respective control surface layout, are shown in Table 1 and Figure 1. The most important characteristics are $p_{c.g.}$ and x_{pilot} as these determine how far the pilot is located from the Center of Gravity (CoG). In the research of van Overeem et al. [8] and Stougie et al. [6], this point was miscalculated, causing the load factor at the pilot station to be underestimated, which will later be shown as a crucial validation parameter. Vugts et al. [19] and Torelli et al. [20] performed flight simulator tests for the Flying V, in which the distance of the pilot station, x_{pilot}, was set to be 26.3m from $p_{c.g.}$ = 31.3m at 55% MAC, leading to x_{pilot} = 5.00 m from the nose of the aircraft.

B. Aerodynamic Model Definition

This section will briefly describe the aerodynamic model used in this research. The aerodynamic model has been directly taken from van Overeem et al. [8]. Firstly, the aerodynamic model limitations are highlighted after which the trimmed condition is shown.

1. Model limitations

The model limitations present in the current research mostly depend on a lack of information about the bare airframe. The aerodynamic model derived from van Cappuyns [7] and Overeem et al. [8] uses linear aerodynamic relations and lacks data for the control surface effectiveness. It is therefore assumed that the inboard elevon, $CS1$, does not influence roll or yaw axes, and $CS2$ and $CS3$ do not affect the pitch axis. The engine model assumes a maximum constant thrust across the flight envelope. As such, the maximum thrust provided in Table 3 is not specified for each flight condition despite the fact that realistically the maximum available thrust changes during flight [21]. Lastly, the inertia remains constant for all CoG values and at minimum landing and maximum take-off weights.

2. Trim condition

For linear analysis, used in tuning and validating the HQ, the trim condition must have zero residual state derivative to avoid changes in any state. It was found that the trim routine, implemented by van Overeem et al. [8] would not bring the aircraft in a trim condition for the prescribed flight condition, so it is uncertain if the results achieved from the linear analysis are accurate. The trim conditions for the two flight conditions considered in this research are shown in Table 2.

Table 1 Flying-V properties [7, 19]

Parameter	Value	Unit
T_{dy}	±5.60	m
T_{dz}	0.800	m
S	883	m^2
c_{MAC}	18.7	m
$p_{c.g.}$	29.4	m
x_{pilot}	5.00	m
b	65.0	m
L	55.0	m
Height	17.0	[m]
Pax	314	[-]
Fuel Capacity	140.000	[l]
Cargo Capacity	160	[m^3]

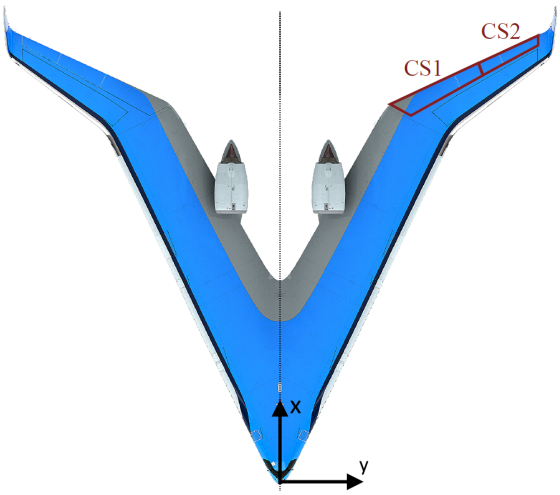

(a) Top view Flying V

(b) Side view Flying V

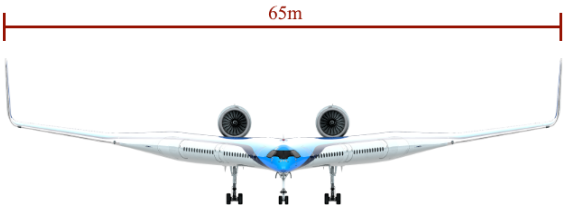

(c) Front view Flying V

Fig. 1 Flying-V: 2 elevon control surface layout [7]

Table 2 Trimmed aircraft states in Approach and Cruise

	$m\ [kg]$	h $[m]$	M [-]	$V_\infty\ [m/s]$	α [°]	$CS1_{L/R}$ [°]	$CS2_{L/R}$ [°]	$CS3_{L/R}$ [°]	$T_{1/2}\ [kN]$
Approach	2.10×10^5	1000	0.200	67.3	23.3	20.1	21.4	0	268
Cruise	2.40×10^5	13000	0.850	250.8	7.01	6.41	9.40	0	124

C. Actuators & Sensors

The actuator and sensor characteristics are crucial parameters for the performance of the control system. Equation 1 illustrates the transfer functions utilized in this study to characterize the dynamics of the control surface, engine, and sensor. These dynamics have been derived from Matamoros & de Visser [22]. It should be noted that the actuator dynamics from Matamoros & de Visser were derived for fighter aircraft. In contrast, conventional large passenger aircraft are typically in the order of ζ_{act} = 1 and ω_{act} = 20 rad/s [23]. In this research, the dynamics derived from Matamoros & de Visser are used with ζ_{act} = 1.11 and ω_{act}= 63.2 rad/s, as used by Stougie et al. [6].

$$H_{act} = \frac{\omega_{act}^2}{s^2 + 2\zeta_{act}\omega_{act}s + \omega_{act}^2} = \frac{4000}{s^2 + 140s + 4000},\quad H_{eng} = \frac{1}{0.2s+1},\quad H_{sens} = \frac{1}{\tau_{filt}s+1}e^{-\tau_d s} \tag{1}$$

Table 3 displays the actuator position and rate limits, as well as the utilized dynamics for each actuator. Next, Table 4 shows the characteristics used in this research. Stougie et al. changed the characteristics of several sensors, indicated by a right arrow, to achieve consistent Level 1 HQs, for the tested requirements [6].

Table 3 Control effector parameters [8, 24]

Control effector	Notation	Actuator limits	Rate limit [°/s]	Dynamics
Outboard Elevon	$CS1_L, CS1_R$	[-25, 25] [°]	80	$H_{act}(s)$
Inboard Elevon	$CS2_L, CS2_R$	[-25, 25] [°]	80	$H_{act}(s)$
Rudder	$CS3_L, CS3_R$	[-30, 30] [°]	120	$H_{act}(s)$
Engine thrust	δ_{T1}, δ_{T2}	$[0, 3.176 \cdot 10^5]$ [N]	-	$H_{eng}(s)$

Table 4 Baseline sensor characteristics [6]

Sensor	Sampling rate [Hz]	Time delay [s], τ_d	Noise $[\sigma^2]$	Bias	Filter time constant [s], τ_{filt}
p, q, r [rad/s]	50	$0.1 \rightarrow 0.04$	$1 \cdot 10^{-9}$	$3 \cdot 10^{-5}$	$0.05 \rightarrow 0.03$
ϕ, θ [rad]	50	0.1	$1 \cdot 10^{-9}$	$4 \cdot 10^{-3}$	0.05
V [m/s]	$\frac{1}{0.065}$	0.325	$1 \cdot 10^{-4}$	2.5	0.05
α [rad]	50	0.1	$7.5 \cdot 10^{-8}$	$3 \cdot 10^{-5}$	0.05
β [rad]	50	0.1	$7.5 \cdot 10^{-8}$	$3 \cdot 10^{-5}$	$0.05 \rightarrow 0.1$
A_x, A_y, A_z [g]	50	0.1	$1 \cdot 10^{-5}$	$2.5 \cdot 10^{-3}$	0.05

III. Controller Structure

As shown by Van Overeem et al. [8], the lateral eigenmodes are unstable, yielding the need for a FCS. To maintain performance and safety, gain scheduling techniques were used to extend the flight envelope [25]. In between these gain scheduling parameters, performance can still not be guaranteed due to non-linearities and uncertainties [26]. Therefore, Slotine & Li [26] proposed nonlinear control techniques, which have served as the foundation for numerous modern control techniques. The current implemented FCS of the Flying V is based on INDI, a feedback linearization technique [6, 8]. This section will give the reader a basic understanding of the control law that has to do with INDI, leading to the implementation of Hybrid INDI.

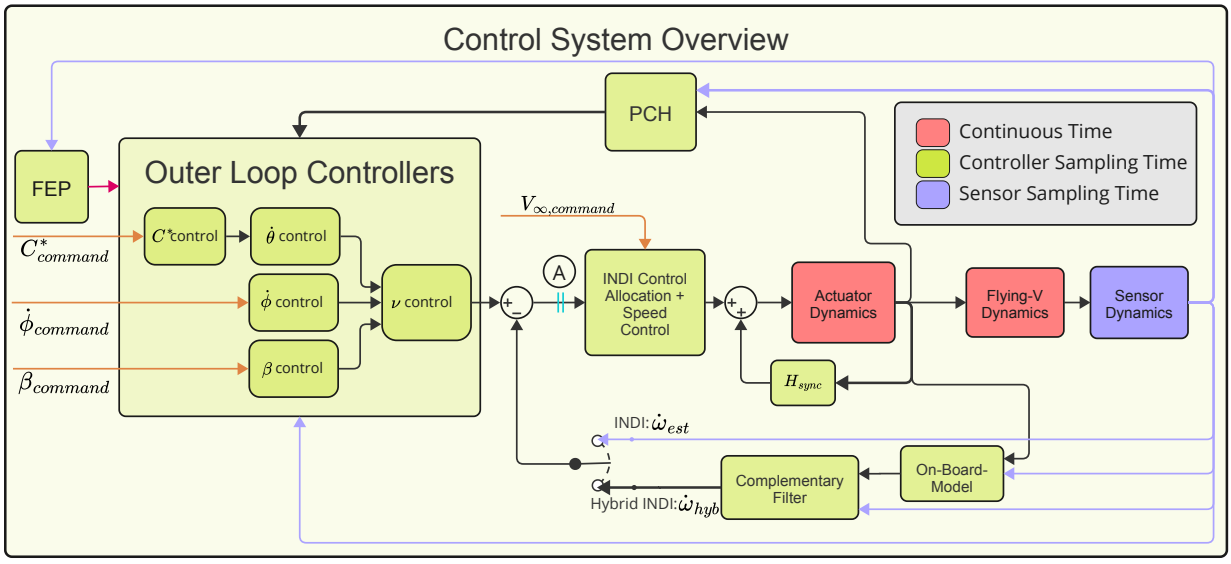

Fig. 2 INDI/Hybrid INDI control system overview

A. Incremental Nonlinear Dynamic Inversion

The basic principle of INDI is strongly related to its model-based counterpart, Nonlinear Dynamic Inversion (NDI). The interested reader is referred to Pollack [23] for an elaborated background and derivation of the NDI control law. While a NDI offers an advantage over conventional linear control laws by simplifying gain scheduling, it is less effective in addressing model mismatch [27]. INDI addresses some of these limitations by reducing the need for a detailed On-Board-Model (OBM). It only requires the control effectiveness terms, which in itself can lead to a complex model [22]. The basic principle of INDI is derived below in Equations 2, 3, 4 and 5 but has been extensively documented in the literature [28, 29]. Consider a general control affine Multiple Input-Multiple Output (MIMO) system, shown in Equation 2.

$$\begin{aligned} \dot{\boldsymbol{x}} &= \boldsymbol{f}(\boldsymbol{x}) + \boldsymbol{G}(\boldsymbol{x})\boldsymbol{u} \\ \boldsymbol{y} &= \boldsymbol{h}(\boldsymbol{x}) \end{aligned} \tag{2}$$

Here, the state vector $\boldsymbol{x} \in \mathbb{R}^n$, input vector $\boldsymbol{u} \in \mathbb{R}^m$ and output vector $\boldsymbol{y} \in \mathbb{R}^m$ are described by the smooth mapping functions, $\boldsymbol{f}, \boldsymbol{G}$, and $\boldsymbol{h}$. A first-order Taylor expansion is taken around the point $\boldsymbol{x}_0, \boldsymbol{u}_0$.

$$\dot{\boldsymbol{x}} = \dot{\boldsymbol{x}}_0 + \frac{\partial}{\partial \boldsymbol{x}} \left[\boldsymbol{f}(\boldsymbol{x}) + \boldsymbol{G}(\boldsymbol{x})\boldsymbol{u}\right]_{\boldsymbol{x}_0,\boldsymbol{u}_0} (\boldsymbol{x} - \boldsymbol{x}_0) + \frac{\partial}{\partial \boldsymbol{u}} \left[\boldsymbol{f}(\boldsymbol{x}) + \boldsymbol{G}(\boldsymbol{x})\boldsymbol{u}\right]_{\boldsymbol{x}_0,\boldsymbol{u}_0} (\boldsymbol{u} - \boldsymbol{u}_0) \tag{3}$$

With INDI it is assumed that the sampling time of the control system is sufficiently high to make the time-scale separation assumption hold, which states that the state-dependent increments $\partial \boldsymbol{f}(\boldsymbol{x})/\partial \boldsymbol{x}$ change an order of magnitude slower compared to the input-dependent increments, $\boldsymbol{G}(\boldsymbol{x})$. Thus, allowing us to neglect the state-dependent terms, as further elaborated upon by Falkena [30]. Stougie et al. studied the effect of the sampling time and concluded that with the set sampling frequency of f_s=100 Hz, the tracking error does not impose problems concerning this assumption [6]. This gives that $\boldsymbol{x} \approx \boldsymbol{x}_0$ [29]. Furthermore, based on the control affinity assumption, the mapping function $\boldsymbol{f}$ representing the system's dynamics is assumed to be independent of the input vector, $\boldsymbol{u}$. The resulting simplified MIMO system from Equation 2 is given in Equation 4, together with the definition of $\boldsymbol{G}(\boldsymbol{x})$ within this research.

$$\begin{aligned} \dot{\boldsymbol{x}} &\approx \dot{\boldsymbol{x}}_0 + \boldsymbol{G}(\boldsymbol{x})(\boldsymbol{u} - \boldsymbol{u}_0) \\ \text{where } \boldsymbol{G}(\boldsymbol{x}) &= \frac{\rho V_\infty^2 Sc}{2} {\boldsymbol{I_C}}^{-1} \begin{bmatrix} C_{l_{CS1_L}} & C_{l_{CS1_R}} & C_{l_{CS2_R}} & C_{l_{CS2_R}} & C_{l_{CS3}} \\ C_{m_{CS1_L}} & C_{m_{CS1_R}} & C_{m_{CS2_R}} & C_{m_{CS1_R}} & C_{m_{CS3}} \\ C_{n_{CS1_L}} & C_{n_{CS1_R}} & C_{n_{CS2_R}} & C_{n_{CS2_R}} & C_{n_{CS3}} \end{bmatrix} \\ \boldsymbol{y} &= \boldsymbol{h}(\boldsymbol{x}) \end{aligned} \tag{4}$$

By assuming $\dot{\boldsymbol{y}} = \dot{\boldsymbol{x}}$, even though there are sensor dynamics, the virtual control law for the INDI loop can be designed. For the body rate control problem, the control law for the actuators can be derived by manipulating Equation 4 into Equation 5. The virtual command signal is defined as the desired $\dot{\boldsymbol{x}}$ and can be chosen to be the rotational body accelerations, $\boldsymbol{\nu} = \dot{\boldsymbol{\omega}}$. Since $\boldsymbol{G}(\boldsymbol{x})$ is a non-square matrix, it will be replaced by $\boldsymbol{\mathcal{B}}^{-1}(\boldsymbol{x})$, which is the Moore-Penrose inversion of $\boldsymbol{G}(\boldsymbol{x})$ [22].

$$\boldsymbol{u} = \boldsymbol{u}_0 + \boldsymbol{\mathcal{B}}^{-1}(\boldsymbol{x})(\boldsymbol{\nu} - \dot{\boldsymbol{x}}_0) \tag{5}$$

Due to the absence of an angular acceleration sensor in the current control system, the rotational body accelerations have to be approximated, which is currently done by differentiating rate gyro measurements using a second-order filter [6]. As stated above, the sensor dynamics are neglected in the derivation above, but cannot be neglected and decrease performance and robustness of the current INDI controller structure [6], which is where Hybrid INDI comes in.

B. Hybrid INDI

Stougie et al. [6] concluded that the desired level 1 HQ cannot be met with the base sensor implementation, given in Table 4. Therefore, the sensor characteristics were adjusted to achieve Level 1 HQs. The biggest problem was low gain and phase margin when breaking the loop at location A in Figure 2. To this end, Hybrid INDI is proposed as a suitable solution to make the system less reliant on the sensor characteristics and achieve a trade-off between sensor- and model-based INDI which has already been highlighted in previous research [16, 17, 31, 32]. The overview of the Hybrid INDI control system for the Flying V is shown in Figure 2. In contrast to conventional INDI, instead of using a second order filter to approximate $\dot{\omega}_{est}$, the knowledge of the aerodynamic model and equations of motion of the system are used to estimate a state derivative of the virtual control inputs. Then using a Complementary Filter (CF), the estimated $\dot{\omega}_{hyb}$ can be combined with the measured body rates to generate a feedback signal for the inner loop.

1. Complementary Filter

The chosen method for this research to combine the body accelerations predicted by the OBM and the body rates measured by the Inertial Measurement Unit (IMU) using the CF. As the name suggests, the CF uses information that complements the advantages and weaknesses of the incoming signals. High-frequency noise from the IMU is attenuated by a low-pass filter, and low-frequency model inaccuracies from the OBM are filtered by a high-pass filter. The schematic overview of the CF used in the Hybrid INDI control system is shown in Figure 4, with the transfer function shown in Equation 6.

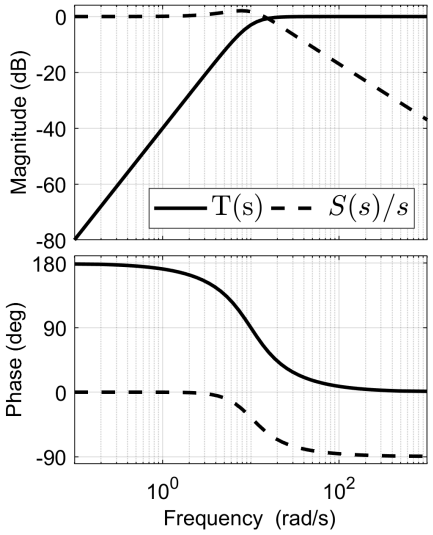

Fig. 3 Frequency response of CF

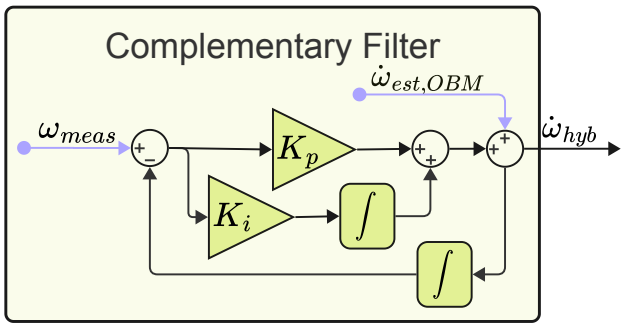

Fig. 4 Complementary Filter overview

This structure has been used by Kim et al. [17] and poses an efficient method to attenuate sensor delay and noise, compared to conventional INDI.

$$\hat{\dot{\boldsymbol{x}}} = \boldsymbol{T}(s)\dot{\boldsymbol{x}}_{obm}(s) + \boldsymbol{S}(s)\boldsymbol{x}_{meas}(s) = \frac{s^2}{s^2 + \boldsymbol{K}_p s + \boldsymbol{K}_i}\dot{\boldsymbol{x}}_{obm}(s) + \frac{(\boldsymbol{K}_p s + \boldsymbol{K}_i)s}{s^2 + \boldsymbol{K}_p s + \boldsymbol{K}_i}\boldsymbol{x}_{meas}(s) \tag{6}$$

The measured body rates, ω_{meas}, coming from the IMU are essentially filtered using a linear *PI* controller, with controller gains, K_p=$2\zeta_{CF}\omega_{n,CF}$ and K_i=$\omega^2_{n,CF}$. The frequency response of a given CF, with $\zeta_{CF} = \sqrt{2}/2$ and $\omega_{n,CF} = 10$ rad/s is shown in Figure 3. The selection of these parameters determines the dependency on either model-based or sensor-based INDI. A higher $\omega_{n,CF}$ will generally give a better response to uncertainties and external disturbances, while decreasing $\omega_{n,CF}$ will counteract the sensor characteristics and will increase phase margins [17, 33]. Within this research, the damping will be set to $\zeta_{CF} = \sqrt{2}/2$, generally considered as a satisfactory damping coefficient. The variable, ζ_{CF}, is fixed to reduce the number of free variables when tuning.

2. Control Allocation

In Equation 4, the smooth mapping function $\boldsymbol{G}(\boldsymbol{x})$, which represents the control surface effectiveness matrix, is inverted to achieve the inner loop control law. However, as three axes are being controlled for the angular accelerations by five control surfaces, the control problem is over-defined, leading to a non-square $\boldsymbol{G}(\boldsymbol{x})$ matrix. Therefore, it is necessary to employ Control Allocation (CA) to solve this problem. The CA scheme used in this research is called Generalized Cascaded Inverses, details on which are available in [6, 34, 35].

The maximum requested incremental control deflections are calculated using Equation 7. Stougie et al. set up different scenarios to take into account control surface saturation. In case of saturation, the respective control surface would be removed from the matrix $\boldsymbol{G}(\boldsymbol{x})$.

$$\Delta\boldsymbol{u}_{max} = \min\left(\dot{\boldsymbol{u}}_{max}\frac{\omega_{act}}{2\zeta_{act}}, \boldsymbol{u}_{max} - \boldsymbol{u}\right) \text{ and } \Delta\boldsymbol{u}_{min} = \max\left(\dot{\boldsymbol{u}}_{min}\frac{\omega_{act}}{2\zeta_{act}}, \boldsymbol{u}_{min} - \boldsymbol{u}\right) \tag{7}$$

After running the algorithm, the matrix $\boldsymbol{G}(\boldsymbol{x})$ is inverted based on the remaining control surfaces. Nominally, the matrix would be inverted using a Moore-Penrose inversion, providing the inverted matrix, $\mathcal{B}^{-1}(\boldsymbol{x})$. If there are saturated control surfaces, this method is adjusted, as the size of $\boldsymbol{G}(\boldsymbol{x})$ would change. For a more elaborated description of this algorithm, the author refers to Stougie et al. [6].

C. Synchronisation Filter

This section describes the implementation of the synchronization filter for the Hybrid INDI control system. Synchronization is necessary to implement INDI, as shown in previous research [36, 37]. Synchronization is needed between the input and virtual command signals as the measured state derivatives provide the controller with a command signal, which is affected by the feedback loop characteristics.

In the control system implemented by Stougie et al. [6], the control surface command signal is synchronized using the same filter dynamics as the one used to acquire the body acceleration signal. The commanded control surface signal is multiplied by the filter dynamics for the virtual command signal, taking into account an additional 2ms, on top of the known body rate sensor time delay, to compensate for the lag due to the filter dynamics and unaccounted delays [6, 28].

The synchronization filter becomes more complex for systems that use Hybrid INDI. As the filtered hybrid signal has to be fed back, the delay introduced by the hybridization filter has to be compensated for. Therefore, the synchronization filter is chosen depending on the method selected for hybridization. As a CF is used in this research, and it is assumed that the input signal is the measured control surface deflection, the used synchronization filter is shown in Equation 8 [32, 33].

$$\boldsymbol{H_{sync}} = \left[T(s) + \frac{S(s)}{s} L(s) \right] e^{-\tau_{sync} s} \tag{8}$$

Here the $T(s)$ and $S(s)$ functions are the same as for the CF, shown in section III.B.1. The function $L(s)$ represents the assumed sensor dynamics $\hat{H}_{sens}$, shown in Equation 1. The tuneable synchronization delay is set to $\tau_{sync} = 0.11s$, considering a unit delay on top of the assumed sensor delay [38].

D. Pseudo Control Hedging

A limitation of conventional INDI is the inability to account for the dynamics and limitations of the control surface actuators. To this end, it is possible to employ Pseudo Control Hedging (PCH), which decreases the virtual command input to scale the input down to a level achievable by the actuators, thereby reducing performance degradation [28, 29]. PCH can be used successfully for certification, as the adaptation is made in the command signal [36]. The hedged virtual command signal is computed by subtracting the virtual command hedge, $\boldsymbol{\nu}_h$, from the desired command signal, $\boldsymbol{\nu}_{cmd}$. The virtual command hedge is computed using Equation 9, obtained from Grondman [36].

$$\boldsymbol{\nu}_h = \boldsymbol{G}(\boldsymbol{x})(\boldsymbol{u}_{cmd} - \boldsymbol{u}_{actual}) \tag{9}$$

E. Outer Loop Controllers

Figure 2 shows that the outer loop is controlled using different linear outer loop controllers. This section will elaborate on the different controllers. Since most controllers remain unchanged compared to the implementation of Stougie et al. [6], only additions and changes are highlighted in this section.

1. C controller*

The control system that has been changed compared to Stougie et al. [6] is the C^* implementation. The C^* control law has been implemented, as pilots cannot control pitch rate and load factor independently [39]. Furthermore, this control law is used in Airbus aircraft, enhancing pilots' familiarity when flying with the Flying V [6, 40]. The C^* controller combines pitch rate and load factor feedback, defined by Equation 10:

$$C^* = \frac{V_{CO}}{g} q + n_{z,pilot} \tag{10}$$

where V_{CO} is the cross-over speed at which pitch rate and load factor are balanced in control input, set to 130 m/s [39]. A compensation term, $\frac{\cos(\theta)}{\cos(\phi)}$, is added as this limits the C^*_{cmd} from the pilot in turns and high pitch attitude [6, 41]. The C^* command is translated into a load factor command at the pilot station, which is limited by the FEP, after which $\dot{\theta}_{cmd}$

is calculated. There have been some modifications to the updated control structure compared to the structure from Stougie et al. [6]. Firstly, the K_{nzs} gain is removed, which operates as an integrator for the C^* controller. However, it was found that this integrator would overflow, as the load factor does not need a C^*_{cmd} to be non-negative. Secondly, the load factor feedback to the controller has to be for the pilot station, which was previously done with the $n_{z,c.g.}$. Next, the feedback before gain K_d must be a gravity component compensation. In the implementation from Stougie et al. [6], 1 g was subtracted from the load factor to calculate the $\Delta n_{z,pilot}$, which gave trimming issues. Lastly, V_{CO} has been implemented, compared to a feedback of the airspeed, as this coincides better with the literature and general purpose of the C^* controller [39].

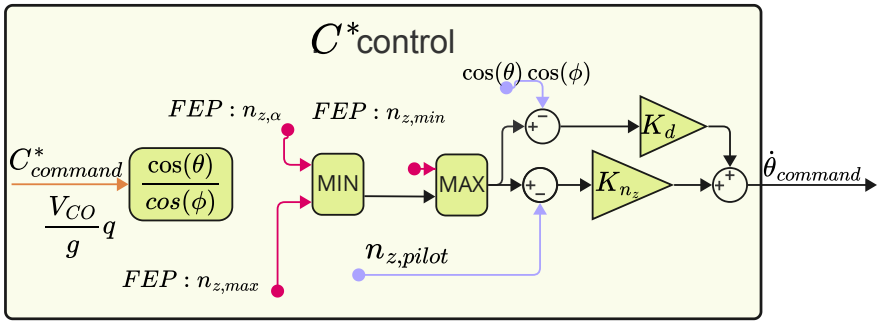

Fig. 5 INDI/Hybrid INDI control system Overview

2. Euler rate & Sideslip controller

The layout for the Euler rate and side slip controller per Stougie et al. [6] has remained the same. The Euler rate controllers are second-order filters with a feedforward term to increase tracking performance [35]. Furthermore, the PCH signal is subtracted from the desired command signal as described in Section III.D. The sideslip controller uses a pilot β_{cmd} and uses the representation of Equation 11, based on Lombaerts & Looye [42].

$$r_{ref} = \frac{1}{V_\infty}\left(wp - A_y\right) - \left[\frac{1}{s}K_{\beta_i}\left(\beta_{cmd} - \beta\right) - K_\beta \beta\right] - r_{meas} \tag{11}$$

3. Linear virtual command controller

The last outer-loop controller converts angular references to virtual command inputs, $\boldsymbol{\nu}$, which are then fed to the inner-loop for dynamic inversion. This linear controller structure has been based on research from Lombaerts et al. [41] and Grondman et al. [36] and implemented by Stougie et al. [6]. Each virtual command input is shown in Equation 12.

$$\begin{aligned}
\nu_p &= \left(K_\phi + \frac{K_{\phi I}}{s}\right)\cdot \phi_{ref} + K_{\dot\phi}\cdot\dot\phi_{ref} + K_{\ddot\phi}\cdot\ddot\phi_{ref} \\
\nu_q &= K_\theta\cdot\theta_{ref} + K_{\dot\theta}\cdot\dot\theta_{ref} + K_{\ddot\theta}\cdot\ddot\theta_{ref} \\
\nu_r &= K_r\cdot r_{ref}
\end{aligned} \tag{12}$$

4. Speed controller

Next to the outer-loop controllers for the virtual command signal, a proportional controller for the thrust control is implemented, using the representation shown in Equation 13.

$$T_{cmd} = K_T\left(V_{\infty,cmd} - V_{\infty,meas}\right) + T_{trim} \tag{13}$$

F. Flight Envelope Protection

Stougie et al. concluded that their implementation for the FEP is not satisfactory, giving overshoot on the α protection [6]. This has been further revealed in piloted flight simulations conducted by Atmaca et al. [9]. The implementation of

Stougie et al. [6] consisted of a linear controller activated when the protected state surpasses a threshold value. In the linear FEP, the protected states are; $n_{z,pilot}$, α and ϕ. The general representation was derived from Lombaerts et al. [41].

This research employs an exponential potential function to implement a command limitation for FEP, following the methodology outlined by Sun et al. [43]. Consider a state, x_1, which will be protected, where its state derivative, x_2, is known, together with the reference signal of $x_{2,ref}$, assuming a rate controller, the implemented FEP is shown in Equation 14. It should be noted that for minimum protection, the minimum value should be smaller or equal to zero.

$$
\begin{aligned}
x_{2,FEP,max} &= x_{2,ref}\left(1-u_p^+\right), \quad \text{where } u_p^+ = \begin{cases} e^{\eta\left(x_1(t)-x_{1,max}+\zeta x_2(t)\right)}, \text{ if } e^{\eta\left(x_1(t)-x_{1,max}+\zeta x_2(t)\right)} \leq 1 \\ r_p^+, \text{ if } e^{\eta\left(x_1(t)-x_{1,max}+\zeta x_2(t)\right)} > 1 \end{cases} \\
x_{2,FEP,min} &= x_{2,ref}\left(1-u_p^-\right), \quad \text{where } u_p^- = \begin{cases} e^{-\eta\left(x_1(t)-x_{1,min}+\zeta x_2(t)\right)}, \text{ if } e^{-\eta\left(x_1(t)-x_{1,min}+\zeta x_2(t)\right)} \leq 1 \\ r_p^-, \text{ if } e^{-\eta\left(x_1(t)-x_{1,min}+\zeta x_2(t)\right)} > 1 \end{cases}
\end{aligned}
\tag{14}
$$

For this representation, two tuning parameters per protected state, namely η and ζ, are similar to a proportional and derivative gain, respectively. Increasing η will increase the margin before the FEP will become active, where the damping coefficient, ζ, will set how strict the FEP will dampen the rate at which the state derivative x_2 is approaching the protected state. Furthermore, there is a design term, $r_p^{+/-}$, which was found to be dependent on which state is protected.

The protected states in this research are load factor, AoA, pitch attitude, and roll attitude. From industry standards, it is clear there is also an overspeed protection, but this is only audible, so it does not have to be implemented in the control law [44]. The limits for each state are given in Table 5, derived from commonly used state protection limits by Airbus [44]. Some state limits depend on the flight condition or coupled states. Starting with the AoA protection, as

Table 5 Protected states and limits for FEP

State	$n_{z,max}$ $[g]$	$n_{z,min}$ $[g]$	α_{max} $[^\circ]$	$\theta_{max}[^\circ]$	$\theta_{min}[^\circ]$	$\phi_{max}[^\circ]$	$\phi_{min}[^\circ]$
Limit	2.5	-1	22-24	30	-15	66/33	-66/-33

was stated by Stougie et al. [6], the limits are dependent on the air density, varying from 22° at approach to 24° at cruise. Furthermore, the roll protection is dependent on the load factor command. For a pure roll input, the limits are set to be ±66°, whereas with a C^*_{cmd}, the limits are set to be ±33°. Therefore, the constant $r_p^{+/-}$ is especially of use for bank protection, as it is chosen to set $r_p^{+/-} = 1 + \frac{5\pi}{180}$, which will bring the limit back from 66° to 33°, with a protection rate of $5^\circ/s$.

IV. Handling Qualities & Tuning

This section will cover the methods of acquiring the results and validating the performance and robustness of the Hybrid INDI control system with enhanced FEP for Flying V. Firstly, the HQ requirements are explained, together with the method of tuning the outer-loop controllers, for which most of the methods are used and derived from Stougie et al. [6]. As this research aims to compare the nominal performance of the Flying V, comparing INDI and Hybrid INDI, this is done for both controllers. Next, the Hybrid INDI is evaluated using parametric uncertainties and tested on how the set requirement changes compared to the nominal system. Lastly, the test cases for the Command Limited FEP are described and the results are compared with the linear-based FEP.

A. Tuning Routine

Similar to the tuning routine of Stougie et al., the input-output response from pilot command to measured state is linearized using the Control System Toolbox from MATLAB ®*. The relevant states are $n_{z,c.g.}$, q, θ, ϕ, and β, all evaluated in a closed-loop response. Furthermore, the virtual command error, point A in Figure 2, is assessed by breaking each loop one by one to provide information about the inner loop margins [23]. The set requirements for the HQ are derived from MIL-STD-1797A [5] and shown in Table 6. Most of the HQs are determined using a Low Order Equivalent System (LOES) approximation, matching the High Order Equivalent System (HOS) frequency response

*https://nl.mathworks.com/help/control/index.html

within a set region of 0.1 - 10 rad/s. For a more elaborate definition of each defined HQ requirement, the reader is advised to read Stougie et al. [6]. A difference from the criterion set by Stougie et al. is the bandwidth criterion, given in Figure 6. Furthermore, Stougie et al. presented the incorrect HQ minima and maxima for several HQs, regarding approach and cruise. Table 6 presents the correct HQ requirements for the selected parameters, indicated in columns B, for cruise and C, for approach [5].

Together with the linear analysis and scoring of the HQ requirements, three different step response tests are done to test Maximum Control Surface Deflection (CS_{max}), Control Surface Activity ($CS_{activity}$), Settling Time (ST), Overshoot (OS). The test cases have remained the same with respect to Stougie et al. [6] to make a direct comparison. The difference is, however, the sideslip tracking of the controller as from tests of the sensor-based INDI control system; it was shown that the control system could not track any reference sideslip angle larger than $|\beta| \approx 3°$. EASA states the need for a steady-heading sideslip of $\beta = 15°$, and thus, this is chosen as the desired step response test [5, CS25.177(c)]. From the trim routine, the lowest-scored systems are combined, and the nominal system is found, for which the results are shown in Table 8.

Table 6 INDI and Hybrid INDI comparison with Base Sensors [5]
Category B: Cruise Category C: Approach

Longitudinal tuning objectives			
Description	**Type**	**Min** B C	**Max** B C
Response to C^* step command of 1.8 (ΔC^*= 0.8) at t = 1 s, T_{sim} = 60 s			
CS_{max} [°]	Min	-	-
$CS_{activity}$ [°/s]	Min	-	-
ST [s]	Min	-	-
OS [%]	Min	-	-
Linear Analysis			
GM ν_q $[dB]$	Constr.	6	-
PM ν_q [°]	Constr.	45	-
ω_{sp} $[rad/s]$	Constr.	- 0.87	-
ζ_{sp} $[-]$	Constr.	0.30 / 0.50	2.0 / 1.3
CAP $[g^{-1}s^{-2}]$	Constr.	0.085 / 0.16	3.6
$score_{LOES}$ $[-]$	Constr.	-	15

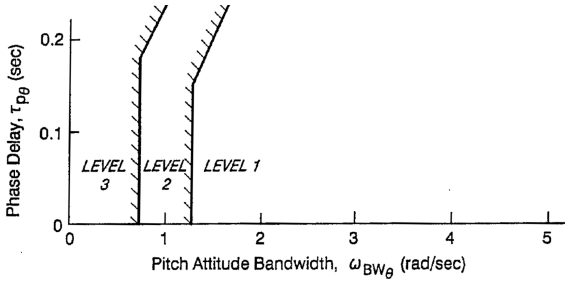

Fig. 6 Bandwidth criteria [45]

Lateral-directional tuning objectives			
Description	**Type**	**Min** B C	**Max** B C
Response to $\dot{\phi}$ block command of $\pm 3°$ at t = 1 - 7s, T_{sim} = 18 s			
CS_{max} [°]	Min	-	-
$CS_{activity}$ [°/s]	Min	-	-
ST [s]	Min	-	-
OS [%]	Min	-	-
Response to β step command of $-15°$ at t = 1 s, T_{sim} = 120 s			
CS_{max} [°]	Min	-	-
$CS_{activity}$ [°/s]	Min	-	-
ST [s]	Min	-	-
OS [%]	Min	-	-
Linear Analysis			
GM ν_p $[dB]$	Constr.	6	-
PM ν_p [°]	Constr.	45	-
GM ν_r $[dB]$	Constr.	6	-
PM ν_r [°]	Constr.	45	-
$1/T_s$ $[s^{-1}]$	Constr.	-0.035 / -0.058	-
T_r $[s]$	Constr.	-	1.4 / 1.0
ω_{dr} $[rad/s]$	Constr.	0.5	-
ζ_{dr} $[-]$	Constr.	0.08	-
$\omega_{dr}\zeta_{dr}$ $[rad/s]$	Constr.	0.15 / 0.10	-
$score_{LOES}$ $[-]$	Constr.	-	15

B. Uncertainty Modeling

Using the nominal tuned system, the Hybrid INDI system is further researched regarding its capability to deal with parametric uncertainties. These uncertainties are shown in Table 7. The Robust Control Toolbox from MATLAB® [†] is used to assess the influence of parameter changes on the requirements shown in Table 6, in time and frequency domain. For the assessment, the control system is linearized and injected with uniformly generated uncertainties within the range. The evaluations are carried out using 750 samples.

Table 7 Uncertain parameters

Parameter	Definition	Uncertainty
I_{xx}, I_{yy}, I_{zz}	Principal inertial parameters	±30 [%]
I_{xz}	Off-diagonal inertial parameter	$\pm 1 \times 10^4 \ \ [kg \cdot m^2]$
m	Mass	$[2.1 - 2.4] \times 10^5 \ \ [kg]$
$\omega_{CS1_L}, \omega_{CS1_R}, \omega_{CS2_L}, \omega_{CS2_R}, \omega_{CS3}$	Actuator eigenfrequency	±30 [%]
$C_{(X,Z,M),CS1}, C_{(Y,L,N),CS2}, C_{(Y,L,N),CS3}$	Aerodynamic control surface effectiveness	±30 [%]
ρ	Air density measurement	±30 [%]
τ_{del}	Body rate sensor delay	[0, 0.080, 0.10, 0.12]

V. Results & Analysis

This section discusses the results of the Hybrid INDI implementation and performance validation compared to the sensor-based INDI model. Firstly, the sensor-based INDI and Hybrid INDI models are compared for the base sensor configuration shown in Table 4. Next, the robustness of the Hybrid INDI controller structure is tested by implementing uncertainties, shown in Table 7 and looking at the influence on time domain step response and frequency domain HQ scores. Lastly, the new FEP implementation is tested using different test cases, comparing it to the linear FEP system.

A. Nominal System Analysis

For the nominal system response of both the sensor-based and Hybrid INDI, the test cases shown in Table 6 are tested. The results for the different requirements are shown in Table 8, where green and yellow colors indicate Level 1 and 2 HQs, respectively. It should be noted that the comparison for INDI is done with an updated control system, compared to what Stougie et al. [6] acquired their results from. The results presented by Stougie et al. [6] were obtained using modified sensor characteristics, but errors in the simulation model affected the assessed performance. Therefore, the results shown in Table 8 for the INDI results are not the same model as per Stougie et al. [6]. The INDI and Hybrid INDI models are both tuned to deliver Level 1 HQ scores and satisfactory time-domain response. Looking at the results from Table 8, there are certain aspects that are evidently different between the INDI and Hybrid INDI control laws.

Firstly, the most significant impact of Hybrid INDI is the increase in phase margin, which is satisfactory for all control axes in both approach and cruise. However, the gain margin for the yaw axis turned out to be low, which is to be expected since in previous research, yaw axis control authority has been found to be unsatisfactory [46]. For the approach condition, the gain margin for the roll axis was found to be low as well, which can be explained by the low control surface effectiveness at low speed and high AoA needed to trim the aircraft, shown in Table 2.

Next, the LOES fit algorithm had difficulty fitting the response of both longitudinal and lateral closed-loop transfer functions, shown in Table 8, to the acquired eigenmode frequency and damping characteristics. This means that the linearisations of the input-output relations cannot fit the same eigenmode characteristics. This is problematic as it can give incorrect HQ results. Since the problem arises especially in approach condition, dynamic characteristics for the Flying V could make the frequency response behave differently to the conventional LOES approximation, which was set up decades ago [5]. The unsatisfactory Control Anticipation Parameter (CAP) and aperiodic roll mode are determined by the LOES approximation and could therefore be computed incorrectly.

For the bandwidth, using the boundaries from Stougie et al., the requirement would not have been met for any flight condition and control law [6]. However, using the revision from Mitchell et al. [45], the requirements are met,

[†]https://www.mathworks.com/products/robust.html

albeit barely for approach condition. It should be noted that the results from Stougie et al. could not be recreated for adjusted sensors and base sensors, and the bandwidth was further decreased with the updated model structure. Due to the inconclusiveness of the validity of this requirement, proper research to valid HQ assessment shall be done to evaluate which HQ shall be used to assess control systems [5, 45, 47, 48].

Looking at the time response characteristics, the implementations of the INDI and Hybrid INDI differ slightly but generally behave similarly. In the approach condition, the response settling time tends to be longer due to control surface saturation, resulting in a lack of control authority. Furthermore, as the integrator term has been removed in the C^* controller, as shown in Section III.E.1, the settling time takes longer than the sensor-based implementation. The most significant difference is the settling time of the sideslip response, where the sensor-based INDI takes 6.5 times longer to settle compared to the Hybrid INDI structure.

Table 8 INDI and Hybrid INDI comparison with base sensors

(a) Longitudinal HQ requirements

Description	Approach		Cruise	
	INDI	**Hybrid**	**INDI**	**Hybrid**
Response to C^* step command of 1.8 (ΔC^*= 0.8) at t = 1 s, T_{sim} = 60 s				
OS [%]	48.9	-18.3	25.4	26.8
ST [s]	41.8	56.2	11.9	4.73
$CS_{activity}$ [°/s]	2.82	1.79	5.40	4.45
CS_{max} [°]	23.8	23.8	9.44	9.52
Linear Analysis				
GM q [dB]	4.80	6.00	5.58	6.78
PM q [°]	32.80	46.3	36.9	49.8
ω_{sp} [rad/s]	2.02	1.89	1.10	1.81
ζ_{sp} [-]	0.673	0.724	0.579	0.870
CAP [$g^{-1}s^{-2}$]	0.111	0.615	0.132	0.345
ω_{BW} [rad/s]	1.65	1.67	1.36	1.84
τ_p [s]	0.184	0.214	0.175	0.197
$score_{LOES}$ [-]	44.5	28.1	26.2	7.78

(b) Lateral-directional HQ requirements

Description	Approach		Cruise	
	INDI	**Hybrid**	**INDI**	**Hybrid**
Response to $\dot{\phi}$ block command of ±3° at t = 1 - 7s, T_{sim} = 18 s				
OS [%]	18.2	24.8	28.5	42.2
ST [s]	5.72	5.40	5.11	5.24
$CS_{activity}$	32.2	37.8	10.6	10.3
CS_{max} [°]	30	30	11.9	11.1
Response to β step command of −15° at t = 1 s, T_{sim} = 120 s				
OS [%]	13.3	17.1	0.749	1.49
ST [s]	64.3	62.1	90.2	13.8
$CS_{activity}$	3.6	5.8	4.77	3.50
CS_{max} [°]	48.7	30	20.7	21.7
Linear Analysis				
GM p [dB]	4.22	4.39	6.20	6.40
PM p [°]	26.1	48.5	35.8	48.8
GM r [dB]	5.25	4.39	5.56	5.33
PM r [°]	35.0	51.3	35.7	46.7
$\frac{1}{T_s}$ [s^{-1}]	0.1088	0.086	0.0425	0.236
T_r [s]	6.549	0.561	0.865	0.801
ω_{dr} [rad/s]	3.702	1.76	1.53	1.83
ζ_{dr} [-]	1.66	0.238	0.387	0.741
$\omega_{dr}\zeta_{dr}$ [rad/s]	0.420	0.492	0.593	1.36
$LOES_{lat}$ [-]	34.3	1.85	11.3	8.74

B. Robustness of Hybrid INDI

This section highlights the influence of uncertainties on the time and frequency domain response for the Hybrid INDI controller. As discussed in Section IV.B, the tuned nominal Hybrid INDI control system is linearized, with parametric uncertainties embedded within the model. These uncertainties are shown in Table 7. Firstly, the influence of the cross-over frequency of the complementary filter, $\omega_{n,comp.filt.}$, is tested on the margins taken at point A in Figure 2, for both model and sensor uncertainties. This will properly indicate the optimal cross-over frequency, considering the

parametric uncertainties. Next, the influence of each uncertainty is given in the frequency domain, indicating which uncertainty has the most influence near cross-over, which impacts stability margins. To demonstrate the robustness in the time and frequency domain, the performance metrics from Table 6 are tested with uncertainties, looking at the boundaries and distribution of the set of requirements.

1. Influence on stability margins

With the implementation of Hybrid INDI, the trade-off between sensor-based and model-based INDI is set with the cross-over frequency of the complementary filter. This is a design variable to achieve satisfactory stability margins. With low $\omega_{n,comp.filt.}$, the CF gives priority to model-based INDI and with high $\omega_{n,comp.filt.}$ there is more priority to sensor-based INDI. As a rule of thumb, the nominal CF cross-over is at the cross-over for the sensor dynamics. For the current inner-loop structure, this gives the dynamics of the body rate sensors, which has its cross-over at $\omega_{filt} = 20$ rad/s. With model uncertainties, it is expected that the stability margins will be lower at low frequencies, whereas with sensor uncertainties, the margins will be lower at high frequencies.

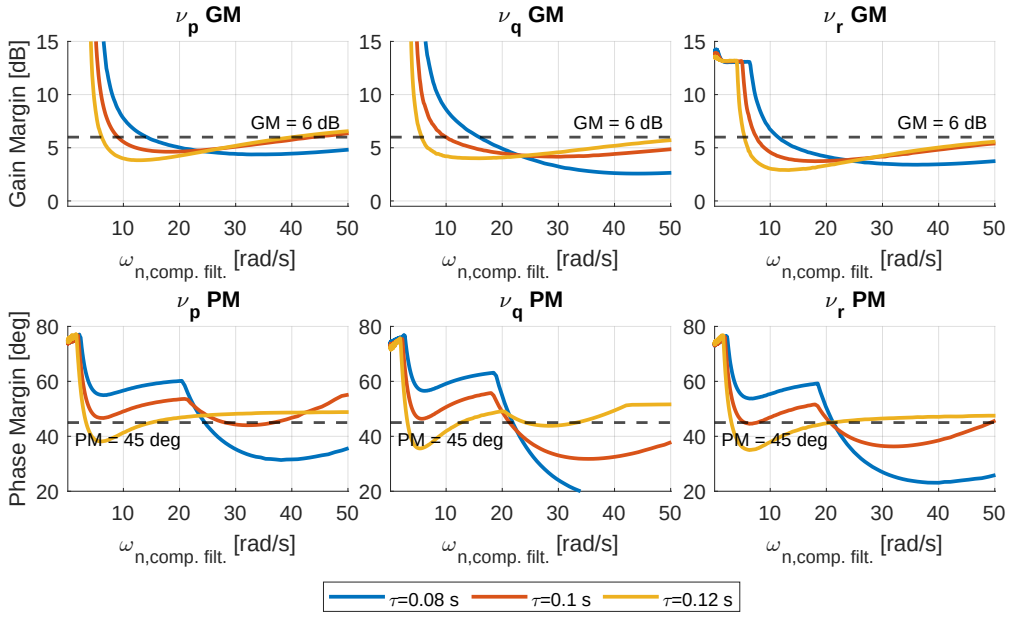

Fig. 7 Sensor uncertainty margins as a function of CF cross-over frequency

Figure 7 shows the impact of the CF for sensor uncertainties, where the time delay and air density measurements are varied. The increments of the time delay uncertainty are given in steps of 2ms, as this is the sampling time of the body rate sensor. If the time delay fits within an integer multiple of the sampling time of the sensor, the margins will be the same. The trend seen in Figure 7 is as expected, where both the gain and phase margins of the different axes are high when the signal relies on the model information. Around the cross-over frequency of the sensor dynamics of 20 rad/s, there is a significant decrease in phase margin, yielding below the level 1 HQs. This drop-off is most noticeable for an underestimation of time delay but remains mostly flat for an overestimation. This can be explained by the compensatory time delay in the synchronization filter, which synchronizes the signal more accurately for an over-estimated time delay, as was shown by Lyu et al. [33]. An interesting point to note is the local minima for the gain margins at low $\omega_{n,comp.filt.}$, indicating that the gain margins depend more on sensor-based INDI. Looking at Figure 8, all the model uncertainties have been sampled, for which it is expected that the control system will become more dependent on sensor-based INDI i.e., a high $\omega_{n,comp.filt.}$. It should be noted that the ideal scenario is tested, where the sensor delay of the body rate sensors is set to $\tau = 0$ s. From Figure 8, it is clear that the preference goes to a high $\omega_{n,comp.filt.}$ when looking at the phase margins. However, this trend is not shown for the gain margins. Especially, the pitch axis seems to perform better when it is dependent on the model-based INDI. Furthermore, the gain margins for roll and yaw both show an anomaly at low $\omega_{n,comp.filt.}$, where there is a sudden decrease in the gain margin but an increase in phase margin, indicating some resonance behavior, which makes the frequency drop-off faster. After this, the margins remain flat, with maximum phase margin, but the gain margins seem to be at a maximum around 7 dB. From these

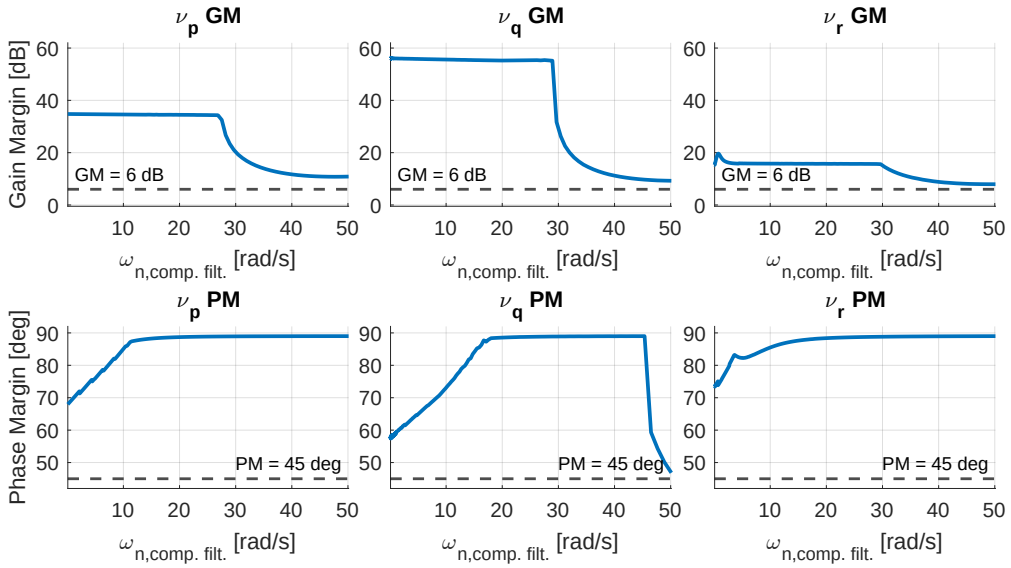

Fig. 8 Model uncertainty margins as a function of CF cross-over frequency

results, to make a proper trade-off, the preference for a low $\omega_{n,comp.filt.} = 8$ rad/s is taken to guarantee satisfactory gain and phase margins for both model and sensor uncertainties. The following results are formed using this $\omega_{n,comp.filt.}$.

2. Uncertain step result

Using 750 samples, the step response for longitudinal, lateral, and directional inputs under uncertain sensor and model uncertainty combinations are tested. The results are displayed in Figure 9 for the provided test cases. The blue line indicates the nominal response of the system to the indicated pilot command input. The shaded grey shows the boundaries of the different response parameters. These results are made for cruise conditions and exhibit similar behavior for the approach. It is evident that the system lacks robustness, as certain combinations of uncertainties can lead to system instability.

Table 9 Percentage of samples within threshold

	C^*_{cmd}	$\dot{\phi}_{cmd}$	β_{cmd}
Approach	90.3 %	82.8 %	87.7 %
Cruise	94.1 %	84.1 %	87.9 %

To quantify the stability of the control system with the given uncertainty samples, a metric is given for how many samples the uncertainty bounds stay within a certain threshold. The Root Mean Squared Error (RMSE) is calculated for the nominal system. Using the RMSE parameter, the threshold is calculated using the function isoutlier()[‡] in MATLAB ®, which filters outliers based on values that are outside 3 Median Absolute Deviation. For each respective variable in Figures 9, the outliers are selected and removed. After this N samples remain, from which the shaded green area is generated. This area represents the minimum and maximum values for each data point, with respect to the sampled uncertainty within the threshold. The percentage of samples that fall within the set threshold per input channel and flight condition are given in Table 9. The results indicate that for more than 80% of the uncertainty combinations, all input channels fall within the set threshold, where the roll rate command shows the least robustness concerning the set parametric uncertainties.

To elaborate upon these results, Figure 10 shows the influence of the different uncertainty parameters at various frequencies. The most critical cross-over region will determine the system's stability. The individual contributions of the different parameters are taken, so no coupling effects are shown. It is therefore assumed that only two parameters

[‡]https://nl.mathworks.com/help/matlab/ref/isoutlier.html

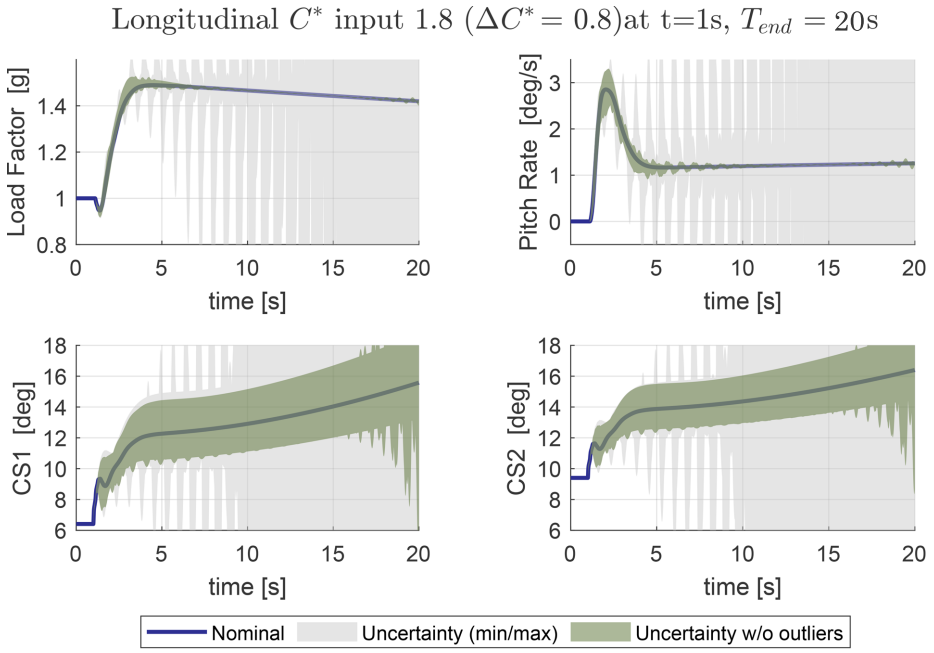

(a) Step response C^*_{cmd}

enhance the uncertainty region where they already contribute. Near the cross-over region, it is interesting that the aerodynamic and inertia uncertainty are the main contributors near the cross-over frequency around $\omega_{c,\nu_p} \approx 5$ rad/s. However, when looking at the phase plot, the aerodynamic uncertainty hardly contributes to this frequency. The phase cross-over might be a more concerning frequency region, around $\omega_{c,\nu_p} \approx 8.5$ rad/s. Here, sensor delay, inertia, and aerodynamic uncertainties contribute to the phase response, whereas time delay dominates the gain. However, as the gain response remains close to 0 dB, this likely leads to the instability. It should be noted that the uncertainty in air density and mass are negligible, looking at the frequency response, which shows that the control system behaves correctly to these uncertainties.

3. Handling Quality uncertainty

To evaluate the robustness of the implemented Hybrid INDI, the HQ requirements given in Table 6 are tested using different uncertain parameter contributions. The results are shown in Figure 11. Each boxplot's lower and upper edges represent the 25th and 75th percentiles, and the blue line indicates the median. The results should be interpreted as follows: all HQ are normalized according to their respective score for the nominal system. For each requirement, the minimum and maximum scores are shown and normalized. For example, for the phase margin requirement of the yaw channel, PM_{ν_r}, the normalized minima are larger than 1, which means the nominal value also does not meet the set requirements. Figure 11 indicates which requirements will likely be met with the set uncertainty parameters. For this simulation, 750 uncertain parameter combinations have been simulated for the cruise condition. From Figure 11, it can be seen that the stability margins, apart from the gain margin for yaw, have the majority of samples meeting the set requirements, as the median is larger than the minimum value. However, there is a large spread with outliers for the phase margins of the system. The same is seen for the approach condition; however, since the nominal values for roll and yaw gain margin did not meet the requirements initially, the result is similar to that of the gain margin of ν_r from Figure 11. Looking at the longitudinal HQ, there are several interesting things to note. Firstly, the LOES approximation of the longitudinal system spans widely, which influences the approximation of the short-period eigenmode. The median is larger than the maximum value, indicating that most of the LOES approximations are unsatisfactory, which should be kept in mind for the following point. Secondly, the eigenmode frequency for a short period is met for most cases. However, the damping is likely to become too large, where the CAP is likely to become too small, indicating a large T_{θ_2}. Lastly, the uncertainties hardly influence the pitch response's bandwidth and time delay parameters. Since these parameters do not depend on the LOES approximation, they possess robustness to uncertainties. For the approach condition, the short period characteristics and CAP stay within the set requirements for the interquartile range. However,

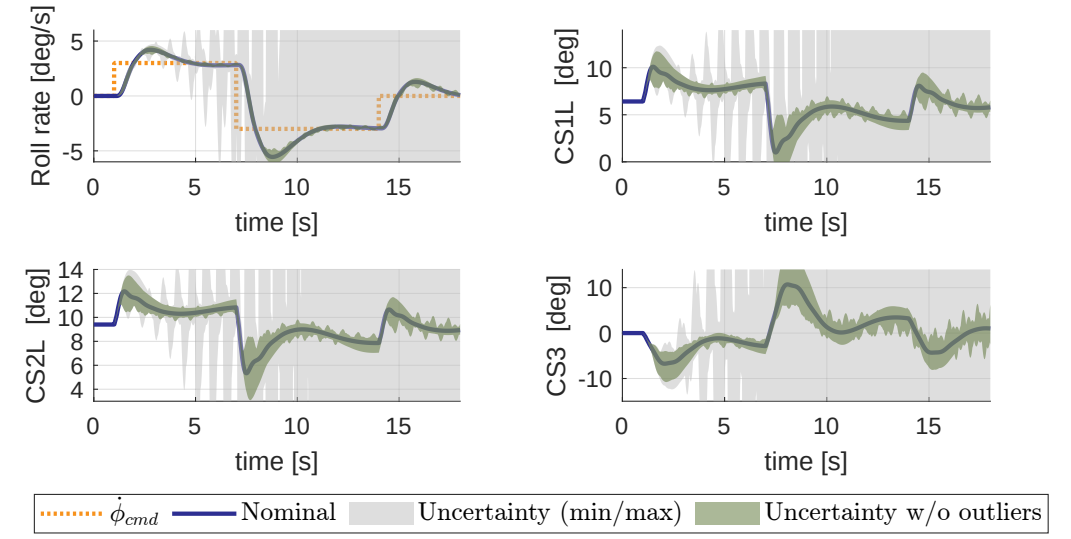

(b) Step response $\dot{\phi}_{cmd}$

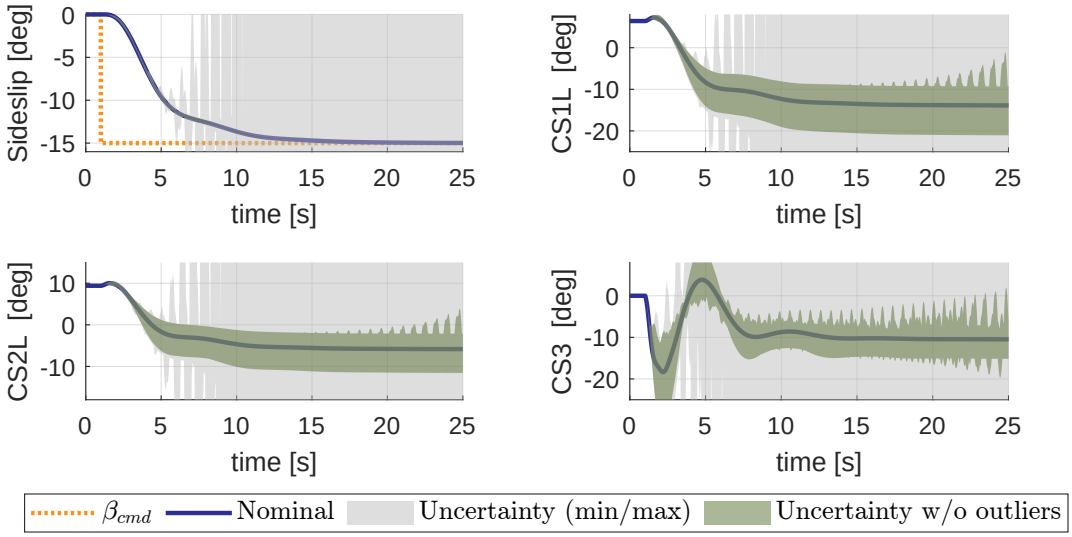

(c) Step response β_{cmd}

Fig. 9 Step response at cruise condition with 750 samples of uncertainty parameters

since the LOES approximation for the approach condition was already unsatisfactory for the longitudinal response, this should be kept in mind.

Lastly, for the lateral HQ analysis, it can be said with more certainty that the set requirements are met as the lateral LOES approximation stays within requirements for most samples, and all mode response requirements are satisfactory for the interquartile range, also concluded for the approach condition.

C. Flight Envelope Protection

The second part of this research focuses on improving the FEP to enhance safety by keeping the protected states within the set limits, as well as removing the overshoot for the AoA as was found by Stougie et al. [6].Further evaluation of the linear FEP revealed that the test cases for the FEP were not severe enough to properly test the safety of the FEP. The test cases from Stougie et al. [6] were:

- Longitudinal command: $C^*_{cmd} = 2$, at $t = 5$ s until $t = 250$ s
- Combined command: $C^*_{cmd} = 2$, at $t = 5$ s until $t = 250$ s, $\dot{\phi}_{cmd} = 5$ deg/s, at $t = 5$ s until $t = 15$ s

A pure roll command has not been used, as it leads to instability for $\dot{\phi}_{cmd} = 5$ deg/s, at $t = 5$ s until $t = 15$ s. Also, since

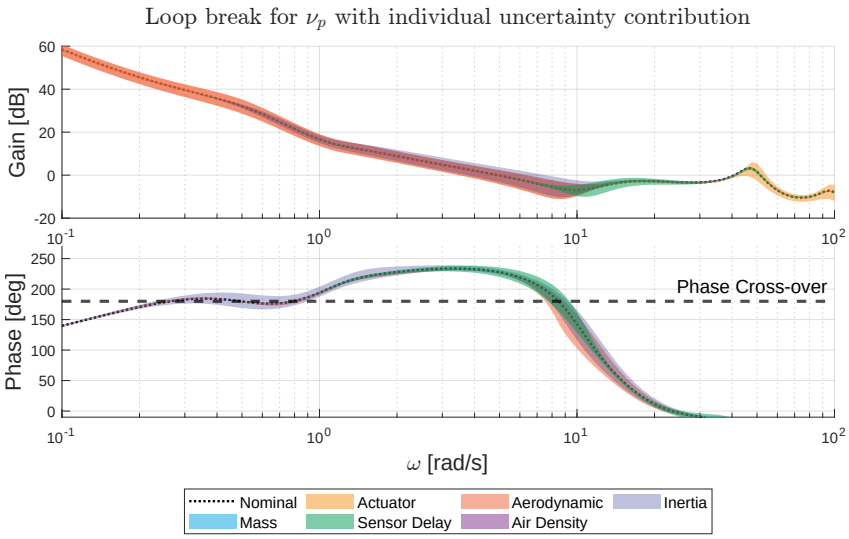

Fig. 10 Broken loop uncertainty at point A for ν_p, with individual uncertainty contribution

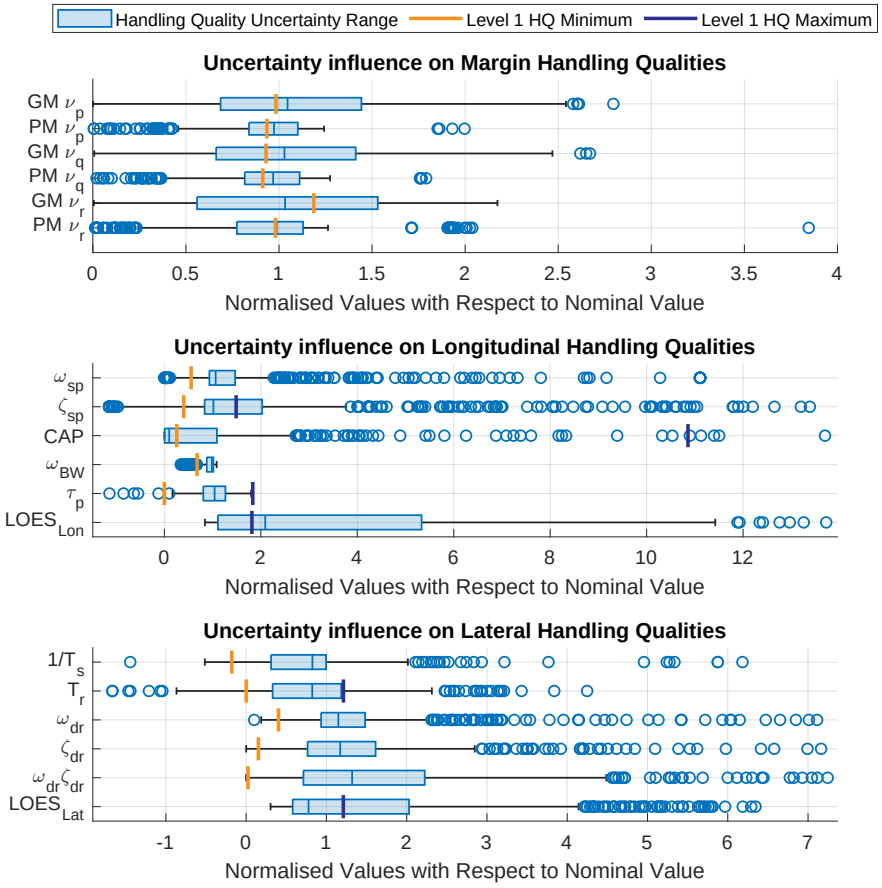

Fig. 11 Boxplots with uncertainties for set HQ requirements in cruise with 750 samples

the limits of the FEP for $n_{z,pilot}$ are set to 2.5g, the author believes a test case should at least consist of a C^* command larger than 2.5. Furthermore, as is given by EASA [49, CS25.147(f)], the aircraft should be able to do a bank-to-bank

from 30 deg until -30 deg under 7 seconds, giving an average roll rate of 8.57 deg/s. As the aircraft starts trim condition, the lateral command will be set to $\dot{\phi}_{cmd} = 20$ deg/s. Therefore, in this research, the following test cases for the FEP are given:

- Longitudinal command: C^*_{cmd} = +3 at $t = 1$ s until $t = 130$ s, C^*_{cmd} = -3 at $t = 130$ s until $t = 150$ s, $T_{sim} = 200$ s
- Lateral command: $\dot{\phi}_{cmd} + -20$ deg/s using 321 step command at $t = 1$ s until $t = 181$ s, $T_{sim} = 200$ s
- Combined command: C^*_{cmd} = +3 at $t = 20$ s until $t = 130$ s, C^*_{cmd} = -3 at $t = 130$s until $t = 180$s and $\dot{\phi}_{cmd} = \pm 20$ deg/s, at $t = 3$ s until $t = 153$ s, $T_{sim} = 200$ s

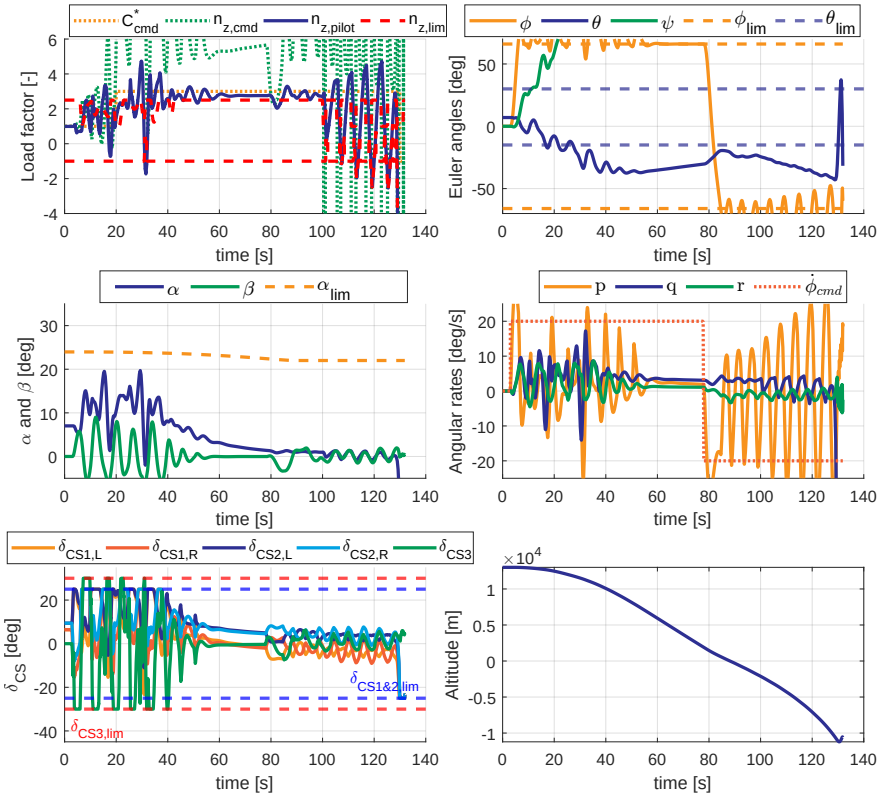

Fig. 12 Linear FEP in Cruise: Combined command

All test cases have been conducted using the Hybrid INDI model, as the revised FEP structure incorporates a model prediction for $\dot{\alpha}$. With the given test cases, none of the linear FEP responses remained stable for both cruise and approach. It proves the linear FEP implementation is not satisfactory. Figure 12 shows an example of such instability, where the linear FEP structure is tested using the combined command input.

Multiple gains could be tuned for the updated FEP, but it became clear that these do not need to be gain scheduled, significantly reducing complexity for multiple operating points. The results for the combined input are shown in Figures 13 and 14 for both cruise and approach, respectively. These results show the improved aspects, limitations, and problems with the newly implemented FEP.

Looking at Figure 13, it is clear that all FEP systems are activated when their respective protected state comes close to the set limit. Starting with α and n_z, since these limits are restricting the $n_{z,cmd}$ which is converted to the $\dot{\theta}_{cmd}$, as shown in Figure 5. When the C^*_{cmd} is given, the initial load factor is increased, for which the load factor limit, $n_{z,lim}$, is decreased to have the load factor stay within boundaries. For the α protection, it can be seen that after a more extended period, for which the θ protection has been active, α reaches its limit, defined as 24 deg at cruise by Stougie et al. [6]. When the α_{lim} is reached, the $\dot{\theta}_{cmd}$ is adjusted, which can be seen by a decrease in θ.

For the θ protection, the system behaves as expected but has a brief overshoot at $t \approx 85$ s, where the pitch attitude increases to $\theta \approx 34$ deg. A coupling between the $\dot{\phi}_{cmd}$ and pitch rate introduces a pitch response when a roll input is given. The coupling is due to the load factor control in the C^* controller as the turn will introduce a load factor at the pilot station, which is not introduced by a C^*_{cmd}. Therefore, the error will be negative, pushing the aircraft down in a turn. In the combined input, when the $\dot{\phi}_{cmd}$ is reversed, this gives a sudden decrease in load factor, from which the

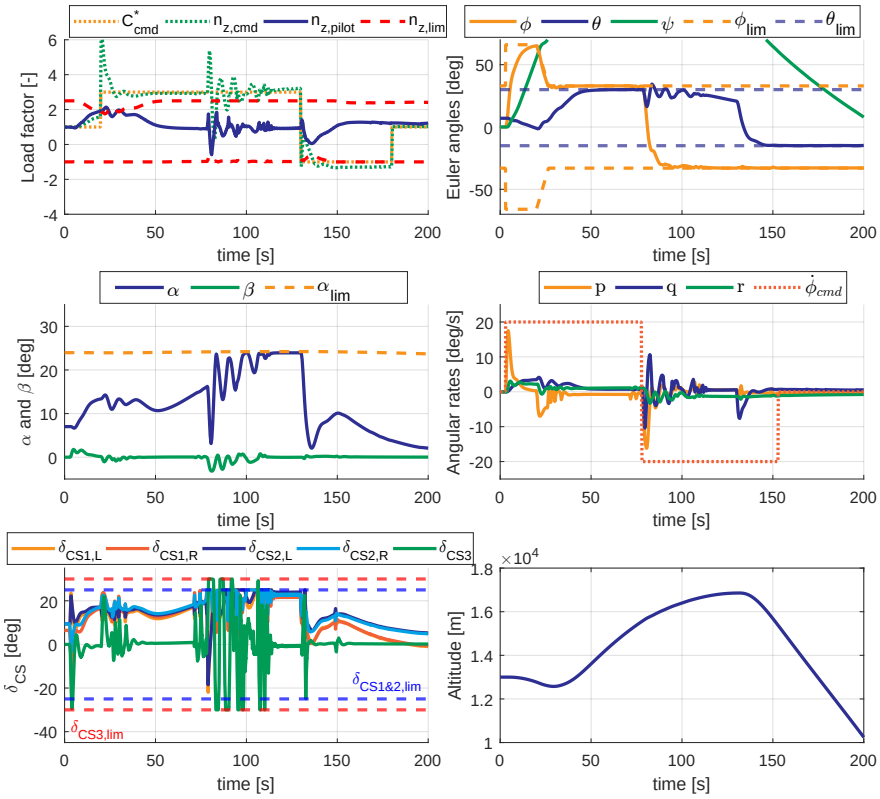

Fig. 13 Updated FEP in Cruise: Combined command

controller responds by pulling the nose up. This is to be expected with the current control structure, but a different controller can be implemented to mitigate this problem. Looking at the ϕ protection, the aircraft steadily approaches the set limit of $\phi_{lim} = 66$ deg. When the C^* command is given, this limit is decreased to $\phi_{lim} = 33$ deg, decreasing with 5 deg/s until reaching -33 deg. It should be noted that the bank-to-bank time satisfies the requirement, reaching $\phi = -30$ deg within $t = 4.42$ s in cruise and $t = 4.465$ s for approach.

Next, the approach condition is shown in Figure 14. It is apparent that protection limits are not satisfied in this condition. The test cases for a pure longitudinal response stay within boundaries, but do not respond to a positive C^* input as the α_{lim} is reached in trim condition. For the lateral and combined inputs, the FEP does not keep the protected states within their boundaries as there is saturation of the control surfaces. When the lateral input command is given, the roll protection keeps ϕ within boundaries. Still, the control surfaces are saturated and cannot protect the other states. However, since there is no longitudinal input, the AoA remains within limits. Due to the coupling of the roll and pitch channels, the pitch protection is therefore exceeded. As for the combined input, as shown in Figure 14, the control surfaces are saturated, with a positive C^*_{cmd}. At $t \approx 100$ s, there is an increase in AoA due to a $n_{z,cmd}$, as the ϕ angle is approaching its protection limit. Due to the coupling of channels, this gives a sudden rise in AoA, which cannot be compensated for as the actuators saturate. For the roll maneuver, when bank angle settles on its limit, the actuators can push the nose of the aircraft down, reducing the AoA and bringing it back to its limit.

VI. Conclusion

This research designs and implements an updated flight control system for the Flying V to enhance the current Flight Control System (FCS), aiming to achieve level 1 Handling Qualities (HQ) based on MIL-STD-1797A standards. For the inner loop, a Hybrid Incremental Nonlinear Dynamic Inversion (INDI) control law using a Complementary Filter (CF) designed with an aim to address stability margin issues caused by time delay. The Hybrid INDI controller showcases superior performance compared to sensor-based INDI. However, due to insufficient gain margin in roll and

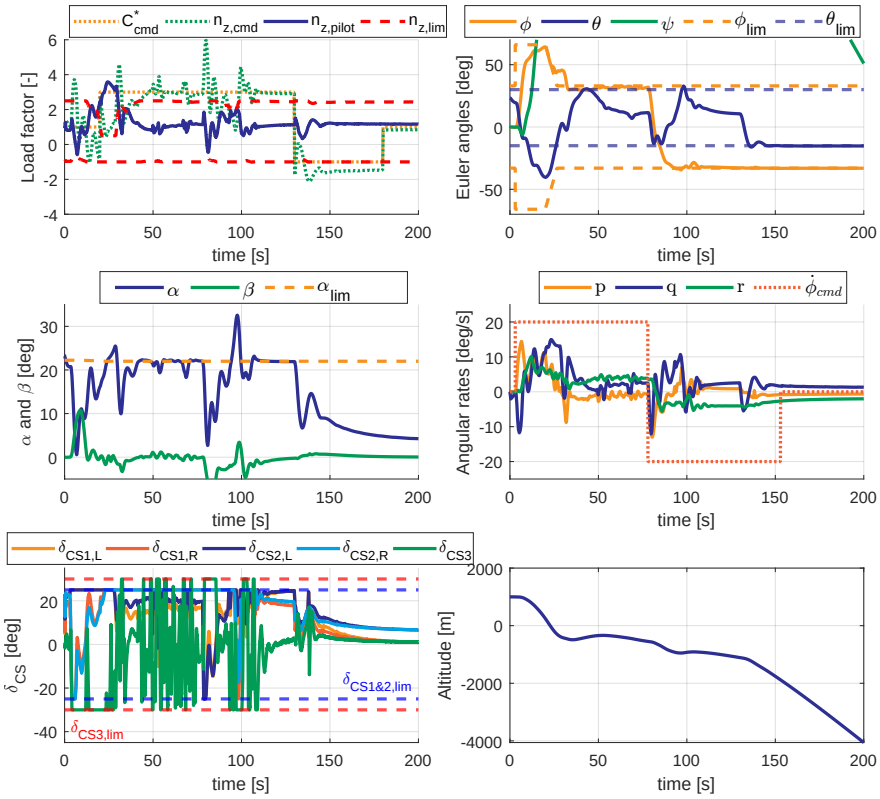

Fig. 14 Updated FEP in Approach: Combined command

yaw channels and exceeding Low Order Equivalent System (LOES) approximation boundaries, further investigation is needed to meet the level 1 HQ criteria. The method used to assess which HQs are used, and their validity for the Flying V use case should be researched further.

Moreover, the study assesses the robustness of the controller under parametric uncertainties, highlighting its limitations in addressing coupled uncertainties such as aerodynamics, inertia, and time delay. While lateral HQ robustness meets satisfactory standards, longitudinal HQ shows less robustness. The fit of the LOES often falls short and dominant for most HQ metrics.

Additionally, the updated FEP introduces an exponential Command Limiting structure to protect load factor, Angle of Attack (AoA), pitch attitude, and roll attitude. Testing reveals the existing linear FEP's unsatisfactory performance when subjected to newly generated, more challenging test cases. The updated FEP improves reliability under cruise conditions but unsatisfactory performance during approach due to actuator saturation.

Additional research is needed to address the validity of the HQ assessment. Moreover, the Control Allocation (CA) scheme, particularly its interaction with the FEP and Pseudo Control Hedging (PCH) structure under actuator saturation, should be researched further, as this is a current limitation.

References

[1] Martinez-Val, R., Palacin, J. F., and Perez, E., "The Evolution of Jet Airliners Explained Through the Range Equation," *Proceedings of the Institution of Mechanical Engineers, Part G: Journal of Aerospace Engineering*, Vol. 222, No. 6, 2008, pp. 915–919. https://doi.org/10.1243/09544100JAERO338.

[2] Liebeck, R., "Design of the Blended Wing Body Subsonic Transport," *Journal of Aircraft*, Vol. 41, No. 1, 2004, pp. 10–25. https://doi.org/10.2514/1.9084.

[3] Oosterom, W., and Vos, R., "Conceptual Design of a Flying-V Aircraft Family," *AIAA Aviation Forum*, AIAA Paper 2022-3200, Chicago, IL, Jun. 2022. https://doi.org/10.2514/6.2022-3200.

[4] Benad, J., "The Flying V - A New Aircraft Configuration for Commercial Passenger Transport," *Deutscher Luft- und Raumfahrtkongress 2015, Rostock*, Deutsche Gesellschaft für Luft- und Raumfahrt, 2015. https://doi.org/10.25967/370094.

[5] "Flying Qualities of Piloted Aircraft," Tech. rep., Department of Defense, United States, Jan. 1990.

[6] Stougie, J., Pollack, T., and van Kampen, E., "Incremental Nonlinear Dynamic Inversion Control with Flight Envelope Protection for the Flying-V," *AIAA SciTech Forum*, AIAA Paper 2024-2565, Jan. 2024. https://doi.org/10.2514/6.2024-2565.

[7] Cappuyns, T., *Handling Qualities of a Flying V Configuration*, MSc Thesis, Delft University of Technology, 2019. URL http://resolver.tudelft.nl/uuid:69b56494-0731-487a-8e57-cec397452002.

[8] van Overeem, S., Wang, X., and van Kampen, E.-J., "Handling Quality Improvements for the Flying-V Aircraft using Incremental Nonlinear Dynamic Inversion," *AIAA SciTech Forum*, AIAA Paper 2023-0105, National Harbor, MD, 2023. https://doi.org/10.2514/6.2023-0105.

[9] Atmaca, D., Stroosma, O., and van Kampen, E., "Piloted Evaluation of Flying-V with Incremental Nonlinear Dynamic Inversion and Envelope Protection," *AIAA SciTech Forum*, AIAA Paper 2025-0973, Jan. 2025. https://doi.org/10.2514/6.2025-0973.

[10] Atmaca, D., and van Kampen, E., "Fault Tolerant Control for the Flying-V Using Adaptive Incremental Nonlinear Dynamic Inversion," *AIAA SciTech Forum*, AIAA Paper 2025-0081, Jan. 2025. https://doi.org/10.2514/6.2025-0081.

[11] Atmaca, D., and van Kampen, E., "Active Incremental Nonlinear Dynamic Inversion for Sensor and Actuator Fault-Tolerant Control," *AIAA SciTech Forum*, Jan. 2026.

[12] Atmaca, D., de Visser, C., and van Kampen, E., "Online Inertial Measurement Unit Fault Identification and Active Fault-Tolerant Flight Control," *Journal of Guidance, Control, and Dynamics*, Vol. 48, No. 10, 2025, pp. 2389–2398. https://doi.org/10.2514/1.G009147.

[13] Asaro, S., Atmaca, D., van Kampen, E., and Vos, R., "Control Surface Allocation Based on Offline Handling Quality Simulations for a Flying Wing Aircraft," *CEAS Aeronautical Journal*, Oct. 2025. https://doi.org/10.1007/s13272-025-00906-2.

[14] Asaro, S., and Vos, R., "Synthesis of the Aerodynamic Model of a Flying Wing Aircraft," *AIAA SciTech Forum*, AIAA Paper 2025-0852, Jan. 2025. https://doi.org/10.2514/6.2025-0852.

[15] Atmaca, D., Stroosma, O., and van Kampen, E., "Design and Piloted Simulation of Envelope-Protected Control for Flying Wing Aircraft," *Journal of Guidance, Control, and Dynamics*, 2025.

[16] Yang, J., and Zhu, J., "A Hybrid NDI Control Method for the High-alpha Super-maneuver Flight Control," *American Control Conference*, IEEE, Boston, MA, Jul. 2016, pp. 6747–6753. https://doi.org/10.1109/ACC.2016.7526734.

[17] Kim, C., "A Hybrid INDI Control for Ensuring Flying Qualities in Failures of Xcg Measurement Subsystem," *Proceedings of the Institution of Mechanical Engineers, Part G: Journal of Aerospace Engineering*, Vol. 237, No. 4, 2023, pp. 972 – 991. https://doi.org/10.1177/09544100221113429.

[18] Sun, D., Hovakimyan, N., and Jafarnejadsani, H., "Design of Command Limiting Control Law Using Exponential Potential Functions," *Journal of Guidance, Control, and Dynamics*, Vol. 44, No. 2, 2021, pp. 441–448. https://doi.org/10.2514/1.G004972.

[19] Vugts, G., Stroosma, O., Vos, R., and Mulder, M., "Simulator Evaluation of Flightpath-oriented Control Allocation for the Flying-V," *AIAA SciTech Forum*, AIAA Paper 2023-2508, National Harbor, MD, Jan. 2023. https://doi.org/10.2514/6.2023-2508.

[20] Torelli, R., Stroosma, O., Vos, R., and Mulder, M., "Piloted Simulator Evaluation of Low-Speed Handling Qualities of the Flying-V," *AIAA SciTech Forum*, AIAA Paper 2023-0907, National Harbor, MD, Jan. 2023. https://doi.org/10.2514/6.2023-0907.

[21] de Zoeten, G. J., Varriale, C., and Vos, R., "Flight Performance Evaluation of the Flying-V," *AIAA Aviation Forum*, AIAA Paper 2023-3484, San Diego, CA, Jun. 2023. https://doi.org/10.2514/6.2023-3484.

[22] Matamoros, I., and de Visser, C. C., "Incremental Nonlinear Control Allocation for a Tailless Aircraft with Innovative Control Effectors," *AIAA Guidance, Navigation, and Control Conference*, AIAA Paper 2018-1116, Kissimmee, FL, Jan. 2018. https://doi.org/10.2514/6.2018-1116.

[23] Pollack, T. S. C., "Advances in Dynamic Inversion-based Flight Control Law Design Multivariable Analysis and Synthesis of Robust and Multi-Objective Design Solutions," Ph.D. thesis, Delft University of Technology, The Netherlands, Oct. 2024. https://doi.org/10.4233/uuid:28617ba0-461d-48ef-8437-de2aa41034ea.

[24] "Type-Certificate Data Sheet for Trent XWB Series Engines, EASA.E.111," Tech. rep., European Union Aviation Safety Agency, Eschenweg, Germany, Oct. 2022. URL https://www.easa.europa.eu/en/document-library/type-certificates/engine-cs-e/easae111-rolls-royce-deutschland-trent-xwb-series.

[25] Åström, K. J., and Wittenmark, B., *Adaptive Control*, Addison-Wesley Series in Electrical Engineering: Control Engineering, Addison-Wesley, Reading, MA, 1989. URL http://www.zentralblatt-math.org/zmath/en/search/?an=0697.93033.

[26] Slotine, J.-J. E., and Li, W., *Applied Nonlinear Control*, Prentice Hall, Englewood Cliffs, NJ, 1991.

[27] Sieberling, S., Chu, Q. P., and Mulder, J. A., "Robust Flight Control Using Incremental Nonlinear Dynamic Inversion and Angular Acceleration Prediction," *Journal of Guidance, Control, and Dynamics*, Vol. 33, No. 6, 2010, pp. 1732–1742. https://doi.org/10.2514/1.49978.

[28] van 't Veld, R., van Kampen, E., and Chu, Q. P., "Stability and Robustness Analysis and Improvements for Incremental Nonlinear Dynamic Inversion Control," *AIAA Guidance, Navigation, and Control Conference*, AIAA Paper 2018-1127, Kissimmee, FL, Jan. 2018. https://doi.org/10.2514/6.2018-1127.

[29] Simplício, P., Pavel, M. D., van Kampen, E., and Chu, Q. P., "An Acceleration Measurements-Based Approach for Helicopter Nonlinear Flight Control Using Incremental Nonlinear Dynamic Inversion," *Control Engineering Practice*, Vol. 21, No. 8, 2013, pp. 1065–1077. https://doi.org/10.1016/j.conengprac.2013.03.009.

[30] Falkena, W., Borst, C., Chu, Q. P., and Mulder, J. A., "Investigation of Practical Flight Envelope Protection Systems for Small Aircraft," *Journal of Guidance, Control, and Dynamics*, Vol. 34, No. 4, 2011, pp. 976–988. https://doi.org/10.2514/1.53000.

[31] Kim, C., Ji, C. H., Koh, G. O., and Kim, B. S., "Stability Margin and Structural Coupling Analysis of a Hybrid INDI Control for the Fighter Aircraft," *International Journal of Aeronautical and Space Sciences*, Vol. 22, No. 5, 2021, pp. 1154 – 1169. https://doi.org/10.1007/s42405-021-00394-8.

[32] Kumtepe, Y., Pollack, T., and van Kampen, E., "Flight Control Law Design using Hybrid Incremental Nonlinear Dynamic Inversion," *AIAA SciTech Forum*, AIAA Paper 2022-1597, San Diego, CA, Jan 2022. https://doi.org/10.2514/6.2022-1597.

[33] Lyu, H., Ye, Z., Chen, Y., Zhao, T., Gong, Z., Liu, X., Qin, B., and Chen, K., "Extended-State-Observer-Based Angular Acceleration Estimation for Supersonic Aircraft Lateral–Directional Control," *Applied Sciences*, Vol. 13, No. 11, 2023. https://doi.org/10.3390/app13116598.

[34] Durham, W., Bordignon, K. A., and Beck, R., *Aircraft Control Allocation*, John Wiley & Sons, Ltd, West Sussex, United Kingdom, Nov. 2016. https://doi.org/10.1002/9781118827789.

[35] Li, M., Li, J., Tang, Y., and Sun, S., "An Extended INDI Approach and Application to Pitch Rate Control Laws Design of an Aircraft," *AIAA Aviation Forum*, AIAA Paper 2021-3005, Online, Aug. 2021. https://doi.org/10.2514/6.2021-3005.

[36] Grondman, F., Looye, G., Kuchar, R. O., Chu, Q. P., and van Kampen, E., "Design and Flight Testing of Incremental Nonlinear Dynamic Inversion-based Control Laws for a Passenger Aircraft," *AIAA Guidance, Navigation, and Control Conference*, AIAA Paper 2018-0385, Kissimmee, FL, Jan. 2018. https://doi.org/10.2514/6.2018-0385.

[37] Pollack, T. S., and van Kampen, E., "Robust Stability and Performance Analysis of Incremental Dynamic-Inversion-Based Flight Control Laws," *Journal of Guidance, Control, and Dynamics*, Vol. 46, No. 9, 2023, pp. 1785–1798. https://doi.org/10.2514/1.G006576.

[38] Smeur, E. J. J., Chu, Q., and de Croon, G. C. H. E., "Adaptive Incremental Nonlinear Dynamic Inversion for Attitude Control of Micro Air Vehicles," *Journal of Guidance, Control, and Dynamics*, Vol. 39, No. 3, 2016, pp. 450–461. https://doi.org/10.2514/1.G001490.

[39] Niedermeier, D., and Lambregts, A. A., "Fly-By-Wire Augmented Manual Control - Basic Design Considerations," *28th International Congress of the Aeronautical Sciences*, ICAS Paper 2012-5.4.1, Brisbane, Australia, Sep. 2012. URL https://www.icas.org/icas_archive/ICAS2012/ABSTRACTS/605.HTM.

[40] Favre, C., "Fly-by-wire for Commercial Aircraft: The Airbus Experience," *International Journal of Control*, Vol. 59, No. 1, 1994, pp. 139–157. https://doi.org/10.1080/00207179408923072.

[41] Lombaerts, T., Looye, G., Ellerbroek, J., and Martin, M. R. y., "Design and Piloted Simulator Evaluation of Adaptive Safe Flight Envelope Protection Algorithm," *Journal of Guidance, Control, and Dynamics*, Vol. 40, No. 8, 2017, pp. 1902–1924. https://doi.org/10.2514/1.G002525.

[42] Lombaerts, T., and Looye, G., "Design and Flight Testing of Manual Nonlinear Flight Control Laws," *AIAA Guidance, Navigation, and Control Conference*, AIAA Paper 2011-6469, Aug. 2011. https://doi.org/10.2514/6.2011-6469.

[43] Sun, D., Jafarnejadsani, H., and Hovakimyan, N., "Command Limiting for Aerial Vehicles With Rate Control Augmentation Systems," *IEEE Transactions on Aerospace and Electronic Systems*, Vol. 57, No. 3, 2021, pp. 1702–1712. https://doi.org/10.1109/TAES.2021.3050674.

[44] Goupil, P., "AIRBUS State of the Art and Practices on FDI and FTC in Flight Control System," *Control Engineering Practice*, Vol. 19, No. 6, 2011, pp. 524–539. https://doi.org/10.1016/j.conengprac.2010.12.009.

[45] Mitchell, D. G., Klyde, H., David, Hoh, R. H., and Aponso, B. L., "Proposed Incorporation of Mission-Oriented Flying Qualities into MIL-STD-1797A." Tech. Rep. WL-TR-94-3162, Wright-Patterson AFB, OH, USA, Nov. 1994.

[46] Joosten, S., Stroosma, O., Vos, R., and Mulder, M., "Simulator Assessment of the Lateral-Directional Handling Qualities of the Flying-V," *AIAA SciTech Forum*, AIAA Paper 2023-0906, 2023. https://doi.org/10.2514/6.2023-0906.

[47] Hoh, R. H., Mitchell, D. G., Ashkqnas, I. L., Klein, R. H., Heffle, R. K., and Hodgkinson, J., "Proposed MIL Standard and Handbook - Flying Qualities of Air Vehicles," Tech. Rep. AFWAL-TR-82-3081.1, Systems Technology, Hawthorne, CA, Nov. 1982.

[48] Gibson, J. C., "Development of a Design Methodology for Handling Qualities Excellence in Fly By Wire Aircraft," Ph.D. thesis, Delft University of Technology, The Netherlands, Feb. 1999. URL http://resolver.tudelft.nl/uuid:6b564b35-cb74-436c-8c47-845bfbbb8b4d.

[49] "Easy Access Rules for Large Aeroplanes (CS-25)," Tech. rep., European Union Aviation Safety Agency, Jun. 2022. URL https://www.easa.europa.eu/en/document-library/easy-access-rules/easy-access-rules-large-aeroplanes-cs-25.